

Trajectory Planning of a Moving Robot Empowers 3D Localization of RFID Tags with a Single Antenna

Anastasios Tzitzis, Spyros Megalou, Stavroula Siachalou, Emmanouil Tsardoulis, Alexandros Filotheou, Traianos Yioultsis *Member, IEEE*, Antonis G. Dimitriou, *Senior, IEEE*

Abstract—In this work, we present a method for 3D localization of RFID tags by a reader-equipped robot with a single antenna. The robot carries a set of sensors, which enable it to create a map of the environment and locate itself in it (Simultaneous Localization and Mapping - SLAM). Then we exploit the collected phase measurements to localize large tag populations in real-time. We show that by forcing the robot to move along non-straight trajectories, thus creating non-linear synthetic apertures, the circular ambiguity of the possible tag's locations is eliminated and 3D localization is accomplished. A reliability metric is introduced, suitable for real-time assessment of the localization error. We investigate how the curvature of the robot's trajectory affects the accuracy under varying multipath conditions. It is found that increasing the trajectory's slope and number of turns improves the accuracy of the method. We introduce a phase model that accounts for the effects of multipath and derive the closed form expression of the resultant's phase probability density function. Finally, the proposed method is extended when multiple antennas are available. Experimental results in a "multipath-rich" indoor environment demonstrate a mean 3D error of 35cm, achieved in a few seconds.

Index Terms—RFID, 3D Localization, Non Linear Optimization, Phase Unwrapping, Trajectory Evaluation, Robotics, SLAM.

I. INTRODUCTION

In the context of our project "RELIEF" [1], we focus on the problem of continuous inventorying in large warehouses and retail-stores. All target products are tagged with passive UHF EPC Gen2 RFID tags. A fixed reader-antenna network, continuously monitoring the entire area, would require a prohibitive installation cost. Instead, we have designed and constructed prototype RFID-equipped robots (see Fig. 1), capable of carrying out the task. The goals of the robots are to be able to construct a map of the "a priori" unknown environment, to navigate autonomously and safely inside it, to interpret their own pose (position and direction) and to identify and rapidly locate all RFID tagged items at cm accuracy and project their locations in the previously created 3D map. In simple words, one would "Plug and Play" a robot in the area and expect a 3D map of the space along with the products.

Manuscript received January 31, 2020

This research has been co-financed by the European Union and Greek national funds through the Operational Program Competitiveness, Entrepreneurship and Innovation, under the call RESEARCH – CREATE – INNOVATE (project code:T1EDK-03032).

All authors are with the School of Electrical and Computer Engineering, Aristotle University of Thessaloniki, Greece, e-mail: antodimi@auth.gr.

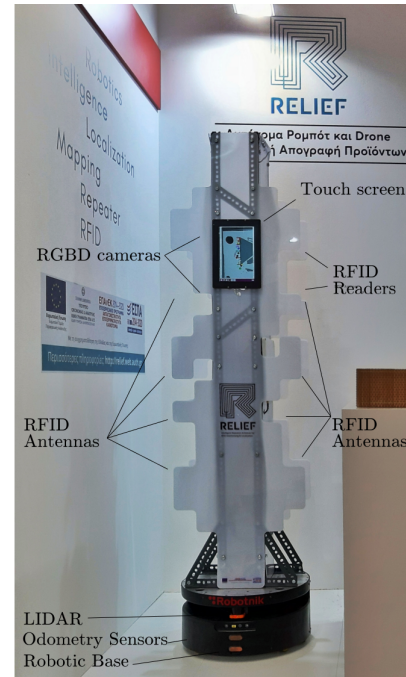


Fig. 1: Photo of "Frida" from a recent international exhibition.

Typical applications may include querying a database for a specific product and get a 3D result pinpointing its location on the map, real-time notifications on the locations of sensitive products, e.g. expired products inside a supermarket, real-time localization of books inside a library etc.

The typical available physical quantities for localization of UHF EPC Gen2 RFID tags are *i*) the backscattered power, usually referred as RSSI and *ii*) the phase of the backscattered signal of each tag. In contrast to RSSI, which can be directly mapped into distance, a single phase sample is useless for localization, due to the 2π ambiguity of phase measurements. However, the robot allows for a dense collection of successive RSSI and phase measurements from different locations, thus forming a "Synthetic Aperture" or "Virtual Antenna Array". In this perspective, the phase information represents a better metric (over RSSI) for localization of the tag, given its tolerance on the tag's antenna polarization, detuning or partial blockage, while experiencing smaller variations due to multipath.

Although localization of RFID tags tends to become a well-studied domain, most of the research has been focused on

the 2D problem, [2]- [8]. Localization in 3D has been proved a quite challenging task. Most of the proposed 3D methods demand the installation of multiple readers and antennas to cover the space of interest [9]- [11]. For satisfactory accuracy, the utilization of an increased number of antennas is required. The cost of such fixed installations, though, is huge and not applicable for large environments, such as warehouses or retail stores.

An alternative solution is to move an antenna in order to collect measurements along a Synthetic Aperture, a technique known from radar systems [12], and now applied in RFID technology. [13] and [14] exploit a single antenna that is moved along two perpendicular directions, by a manual motion controller. The drawbacks here arise from the fact that each tag requires the adjustment of the antenna at a specific position, so it can move along a desired direction, at the expense of time and effort.

Replacement of motion controllers by RFID-equipped robots, provides a sense of automation. A moving robot is capable of covering any space, no matter how large it is. By adjusting its moving strategy, it can collect an infinitely large number of measurements at many closely-spaced antenna locations. [15] - [22] adopt the Maximum-Likelihood (ML) approach and seek the best values over a grid of possible tag locations. Their computational cost is proportional to the grid's dimensions and especially for the case of 3D problems the estimation-time is uncontrollably increased. As a result, all algorithms fail to accomplish real-time results for realistic tag populations and 3D spaces, due to the size of the grid. Most importantly though, localization in three dimensions is only proposed by exploiting multiple antennas at different heights, generating a multi-antenna synthetic aperture.

A different approach is to explore fingerprinting methods, where localization of the unknown tags is carried out by evaluating the resemblance of their measured characteristics (RSSI and phase) with measurements of reference tags, placed at known locations, collected from the same equipment at the same time. Starting from "Landmarc" [23], [24] and [25] exploit RSSI and phase measurements obtained by a RFID-equipped robot, while they propose real-time performance evaluation by further exploiting the reference tags. "Fingerprinting" methods require a long preliminary preparation of the environment due to the need of knowing the absolute position of all reference tags, while their accuracy strictly depends on the density of the reference grid.

Two different approaches were presented in [26], [27]; yet [27] requires functionality of the tag's antenna over large bandwidth and it cannot be applied in real-time for large populations, while [26] represents an interesting alternative to the problem, though it should be extended in 3D.

In contrast to typical SAR-based methods, this work **solves the 3D localization problem by a single antenna**. Instead of placing multiple antennas at different heights, we determine a specific motion-strategy of the robot and thus of the produced "Synthetic Aperture". More specifically, it is proven analytically and verified experimentally that when the robot moves along non-straight trajectories, thus creating curved or generally non-linear synthetic apertures, the circular ambiguity

of the possible tag's locations is eliminated. The proposed motion strategy can be applied to any other SAR method. In this work, we apply "Phase ReLock", [28], a method which transforms the original ML problem into a new equivalent form, which can be solved **rapidly** by standard iterative optimization techniques (instead of searching on a grid). To achieve that, we perform "phase unwrapping" on the measured backscattered phase samples, "correcting" the phases for each tag to take continuous values, instead of being constrained in 2π intervals.

The basic idea was briefly presented in [29]. In this work, we investigate how the motion strategy affects the expected 3D localization accuracy. Firstly, we introduce a "reliability" metric, which evaluates the accuracy of each estimation. Secondly, we investigate how one can set the motion strategy during inventorying, in order to improve the localization accuracy, given real-time knowledge of the reliability-metric. Thirdly, it is shown that by increasing the "curvature" of the path and the amount of turns, the 3D-localization accuracy (and the reliability metric) is improved. Fourthly, we introduce a new phase-model, which accounts for multipath and measurements' errors. We derive the **closed form** probability and cumulative density function of the resultant expected phase under multipath conditions as a function of the ratio ρ of the magnitudes of the "multipath" to the "direct" component. Then, we demonstrate how one can set the motion strategy for increasing "multipath" (larger ρ), in order to maintain a desired reliability. Fifthly, we extend the proposed method, when measurements from multiple antennas are available.

Finally, we present a new set of experimental results, collected by four antennas placed on top of our robot. The robot creates a 3D map of the environment, localizes itself in it and then localizes all surrounding tags. Therefore, the robot's localization/mapping error propagates into the tags' localization error. 3D localization by each antenna is derived separately. When tags are identified by more than a single antenna, combination of the estimations greatly improves the performance. However, 3D estimation can still be delivered even when measurements by a single antenna are available. 3D accuracy in the order of 35cm is accomplished.

The localization method is presented in Section II. The reliability metric, the phase model and the analysis of the relation between the trace of the robot and the localization accuracy are introduced in Section III. Measurements are presented in Section IV, while the extension for multiple antennas is given in Section V. Finally, section IV concludes our findings.

II. 3D LOCALIZATION BY A SINGLE-ANTENNA

Consider a robot carrying an EPC Gen2 UHF RFID reader, connected to one (or more) antenna(s), interrogating passive RFID tags in the surrounding environment. The motion of the robot leads the antenna to a formation of an antenna array $\mathbf{A} = [A_1, \dots, A_N]$ consisted of N locations $A_i = (x_i, y_i, z_i)$, as shown in Fig. 2; z_i is a constant for denoting the specific antenna's height. The distances between a static tag and the

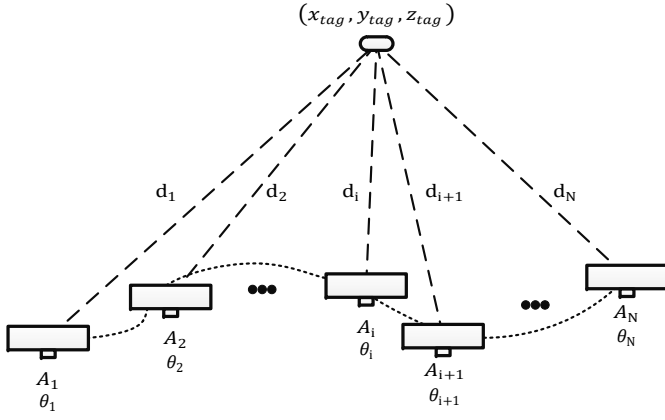


Fig. 2: Geometry of a single-antenna synthetic aperture produced by a moving robot.

antenna locations are $\mathbf{d} = [d_1, \dots, d_N]$, where d_i is the Euclidean distance

$$d_i = \sqrt{(x_i - x_{tag})^2 + (y_i - y_{tag})^2 + (z_i - z_{tag})^2}. \quad (1)$$

$A_{tag} = (x_{tag}, y_{tag}, z_{tag})$ corresponds to the unknown coordinates of the tag.

The set of the phase observations of the backscattered signal is $\boldsymbol{\theta} = [\theta_1, \dots, \theta_N]$, where θ_i is the measured phase recorded at A_i . The measured phase takes values in 2π intervals, which correspond to $\lambda/2$ changes of the antenna-to-tag spatial distance; λ stands for the wavelength of the carrier frequency.

Similarly, $\boldsymbol{\phi}_{wrap} = [\phi_1, \dots, \phi_N]$ is the set of expected phase values produced by the theoretical model

$$\phi_{wrap} = \left(\frac{2\pi}{\lambda} 2\mathbf{d} + c \right) \bmod 2\pi, \quad (2)$$

The RF signal traverses a spatial distance of $2d$ due to the forward and backward communication link. Beyond the term corresponding to the wave propagation, both the tag's and the reader's electronics introduce an additional phase offset, denoted as c . This term is considered constant for the same RFID system (antenna-tag), but yet unknown. Furthermore, the modulo operation has been added to indicate the mapping of the phase measurements in 2π intervals every $\lambda/2$ distance-changes.

A. Formulation of the Optimization Problem

In general, our target is to find the unknown parameters of the theoretical model (2) so that the expected values $\boldsymbol{\phi}_{wrap}$ have best match to the measured ones $\boldsymbol{\theta}$. This is a common problem of data fitting; i.e. the construction of a model (in sense of estimating the values of the model's unknown coefficients) so that it fits best to a series of experimental data. A proper objective function, also called as cost function, expresses the deviation between the two sets. A standard cost function is the one based on the least squared approach. According to it, the best fit is the one that **minimizes** the sum of squared differences between the two sets.

In our case the least squared-based objective function is given by

$$F(x_{tag}, y_{tag}, z_{tag}, c) = \sum_{i=1}^N [\phi_i - \theta_i]^2 \quad (3)$$

If (2) is substituted in (3), the result is a non linear model with four unknown coefficients: the tag's coordinates $(x_{tag}, y_{tag}, z_{tag})$ and the offset term c .

In most non linear models, a closed-form solution is not feasible as in linear cases, and iterative algorithms are deployed; e.g. Steepest Descend, Newton's Direction, Levenberg-Marquardt algorithm, Trust Region method [33]-[37]. Such algorithms require some initial estimation of the unknown parameters to start from. Then, in each iteration those values are refined to improve the fit and decrease the amplitude of the objective function, i.e. F in (3). When some pre-specified convergence criteria are met and a minimum of (3) is reached, the iterative procedure ends. The performance of the optimization though, strictly depends on the curvature of the involved cost function. The existence of multiple local minima (and maxima) can be proved destructive for any deployed algorithm, resulting in the convergence to one of the local minima, instead of the global one, depending on the initial values of the parameters.

The curvature of the objective function at its current form (3), leads to the construction of a non convex optimization problem. Consider the antenna's trajectory of Fig. 3 (a). The cross represents the tag's location and the dashed line joins the tag with the antenna array and is perpendicular to the latter. Fig. 3 (b) represents cost function (3) shown in 2D slices, one at each plane. As it is indicated by the abrupt color changes, the function suffers from multiple local minima (intense blue) and maxima (intense red) and hence, no optimization algorithm can ensure that it will identify the global minimum over a local one. In fact, this depends only on the initial values of the parameters.

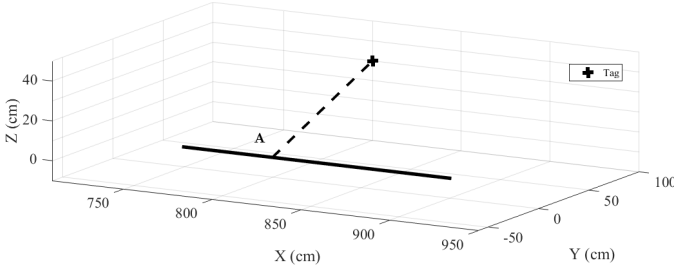
A certain, but inefficient, solution would be an exhaustive search over the parameter-space. In this case, a grid of possible values for each of the unknown parameters would be required to find those that minimize (3). To ensure sufficient localization accuracy, the grid has to be dense and large enough. However, the number of calculations needed is proportional to the size of the grid. The bigger the number of possible values, the higher the algorithm's complexity and execution's time, making the grid-based approaches unqualified for real time applications.

In order to avoid a calculation's grid, we modify the initial optimization problem to ensure convexity and convergence to the global minimum. This is achieved by unwrapping the measured phase curve and adapting the theoretical phase model accordingly:

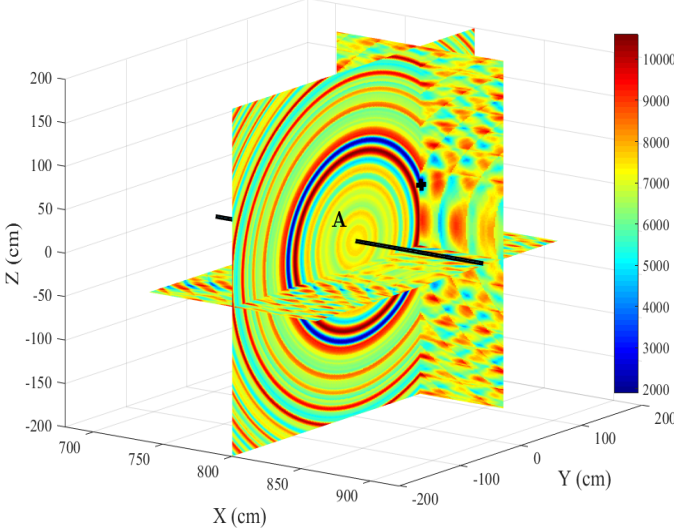
$$\phi_{unwrap} = \left(\frac{2\pi}{\lambda} 2\mathbf{d} + c \right) \quad (4)$$

The modified objective function is

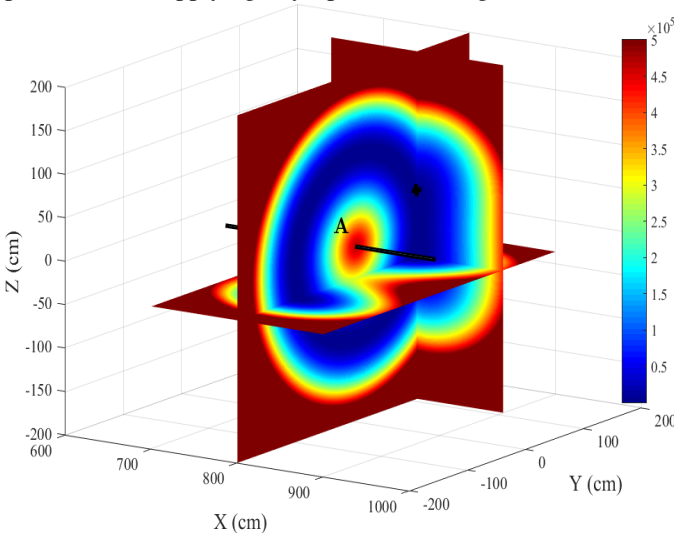
$$F(x, y, z, c) =$$



(a) The location of a tag (cross) and a straight antenna array (solid line). A is the point of the array where the tag-to-antenna is minimum. The dashed line joining A and the tag's location is perpendicular to the antenna array.



(b) Objective function (3). The abrupt changes of color indicate the existence of local minima and maxima, an effect that prevents from applying any optimization algorithm.



(c) Modified objective function (5). Phase Unwrapping "corrected" its shape and eliminated local extrema, allowing for convex optimization.

Fig. 3: Cost functions generated by a straight synthetic aperture. The functions are depicted by 3 slices on X-Y, Y-Z and X-Z plane. A straight path generates a circular locus of possible tag locations, leading to ambiguity regarding the 3D tag's location.

$$\sum_{i=1}^N \left(\frac{4\pi}{\lambda} \sqrt{(x_i - x)^2 + (y_i - y)^2 + (z_i - z)^2} + c - \theta_i^U \right)^2 \quad (5)$$

where θ_i^U denotes the unwrapped phase measurements. The result of this processing is illustrated in Fig. 3 (c). The repetitive shape of (3) has now been "corrected" and the local extrema have been eliminated. The optimum parameters of our model are now the solution of the minimization problem

$$(x^{opt}, y^{opt}, z^{opt}, c^{opt}) = \arg \min_{x,y,z,c} F(x, y, z, c) \quad (6)$$

B. Utilization of Non Straight Synthetic Apertures

Before proceeding to the solution of the optimization problem though, another major issue has to be resolved. It was demonstrated in [29] that a straight single-antenna aperture is incapable of solving the 3D localization problem. The solution, derived by any Maximum-Likelihood method, is satisfied by all points along a specific circle. The circle is perpendicular to the straight axis of the synthetic aperture and centered at the point of the trace, where the tag-to-antenna distance is minimum. All points on that circle, due to their common geometrical relationship with the synthetic aperture, would produce identical set of phases $\phi = [\phi_1, \dots, \phi_N]$ and an identical amplitude of the corresponding objective function.

This effect of the rotational symmetry around the antenna's path is represented by the y-z slices of Fig. 3 (b) and (c), for functions (3) and (5), respectively. The slices are through the perpendicular (dashed) line of Fig. 3 (a), joining the tag's true location and the straight antenna array. The points resulted in same amplitudes of the cost function and denoted by same colouring, form circles around the antenna's path. Even if a ML method accomplishes to find the "best" solution, this will correspond to more than one tag locations, a circular-formed locus in particular. So practically, when straight synthetic apertures are utilized, the output of any applied localization algorithm, is the radius of a circle, perpendicular to the line of motion, where the tag may be located.

It is proven theoretically in the Appendix, that an additional straight synthetic aperture along a different direction, reduces the locus of possible tag locations to only two points. These possible solutions would be symmetrical in relation to the antenna's height; i.e. the $z = z_i$ plane. Consider the non straight trajectory of Fig. 4 (a), which is a combination of two straight paths depicted by red and black color, respectively. Fig.4 (b) and (c) verify our claim for both cost functions (3) and (5). Both slices are again through the two perpendicular (dashed) lines joining the tag's true location with the two sub-paths and intersect on the tag's location. One can notice that the rotational symmetry has been eliminated and circles of same coloring are no longer formed. The lowest value now corresponds to only two symmetrical points, released at the intersection of the shown 2D slices and marked as black and red crosses.

1) *Selecting initial parameter values:* Any optimization algorithm can be deployed to (5) and converge to the proper solution, given that the initial point of the recursive procedure, (x_0, y_0, z_0, c_0) , is chosen properly. First of all, x_0 and y_0

should belong to the half-plane that the antenna illuminates. This is trivial, since the antennas used in most RFID applications are directional patch antennas, which radiate only in one side. Thus, they scan a specific region, depending on the side of the robot the antenna is attached to and the robot's trajectory. Secondly, the value c_0 does not affect the algorithm's convergence and can take any value. On the contrary, as for the initial value of the unknown parameter z_0 , the issue of two solutions existing, as described earlier, requires that z_0 should belong to the correct half-space. This implies necessity of prior information about the spatial configuration of the tags; i.e. whether the tag is placed higher or lower than the antenna's height. However, we often lack such knowledge,

This ambiguity is applied to any SAR-based method and cannot be solved by means of data-processing. In order to eliminate this ambiguity, we should eliminate the symmetry of the antenna's radiation pattern along the z -axis. A possible way to achieve this is to place the antenna at a small height and tilt it upwards (or place it at larger height and tilt it downwards) to ensure that it illuminates a sub-space that is either above or below its height. Typical reader antennas have less than 90° half-power beamwidth (typically around 70°); thus by tilting the antenna at 45° from the horizon, one can illuminate only one quarter of the entire space, eliminating the height ambiguity. This method would not completely prevent the antenna to read tags placed in the undesirable space, but the collected measurements would be few and could easily be discarded. In the experiments, we considered the half-space known.

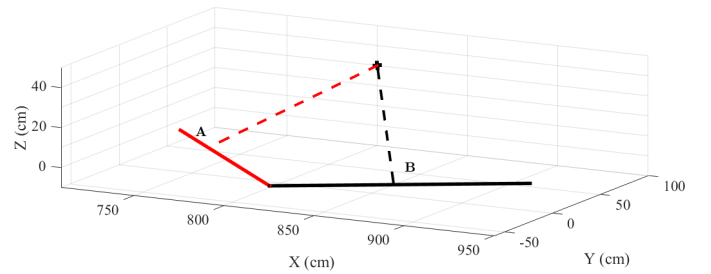
III. PERFORMANCE ASSESSMENT

A. Introduction of Reliability Metric

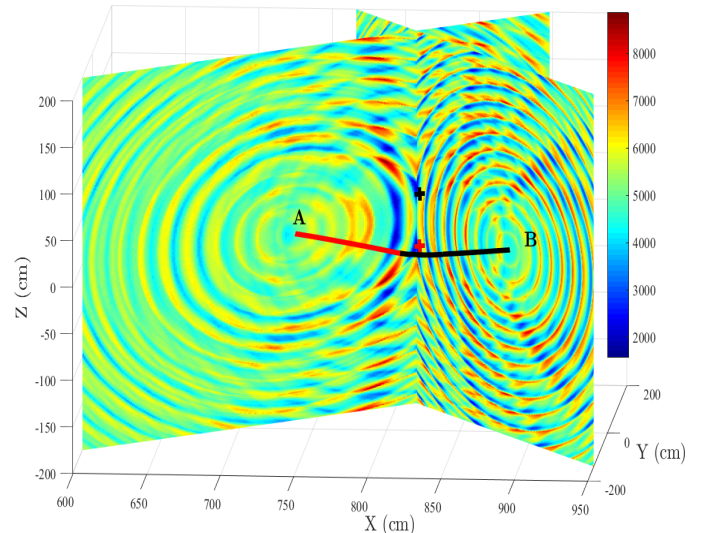
There are cases, when poor localization accuracy is expected. This may result from *i*) an inadequate collection of measurements, *ii*) measurements that suffer from strong multipath and/or noise, *iii*) failure of the phase unwrapping process and in the context of this paper, *iv*) unsuitability of the antenna's trajectory. We aim to define a metric, capable of evaluating the trustworthiness of the estimation. In order to derive the proposed **reliability metric**, we will exploit the local curvature of the cost-function (5) near the estimated solution (near the global minimum).

A standard measure of precision in statistics and optimization is the coefficient's **variance** around its best-fit value. More specifically, it represents how much the estimated value can change away from the optimum and still result in a fit, almost as good as before. High variance means that an equivalently good fit can be achieved by any point in a large area around the optimum point, and hence the latter can not be well identified.

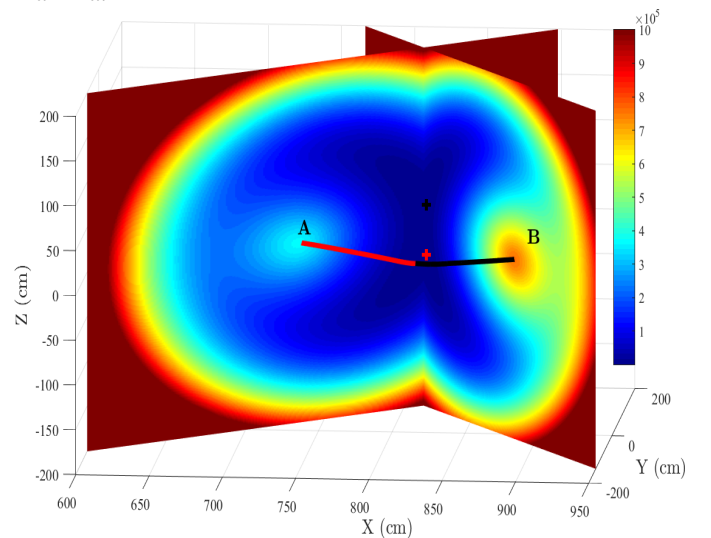
For better intuition, let's examine the following example. Consider the relaxed two-variable problem of (5), where x and y are now the only unknown parameters and z and c are considered known. The optimization problem is solved for two data sets, each of which leads to same solution (x^{opt}, y^{opt}), through cost functions $F1$ and $F2$, respectively. $F1$ is generated by a set of measurements, collected from a tag during one of our experiments, and $F2$ after the same set is



(a) Tag's location (cross) and a non straight antenna array (solid line), consisted by two straight ones. A and B are the two points of each straight sub-path, where the tag-to-antenna distance is minimum.



(b) Objective function (5), shown in $y - z$ slices. The abrupt changes of color indicate the existence of local minima and maxima.



(c) Objective function (5), shown in $y - z$ slices, after phase unwrapping. Phase Unwrapping leads to a convex optimization problem.

Fig. 4: A non straight synthetic aperture, generated by a non straight robot's path, eliminates the rotational symmetry in y - z plane and reduces the locus of possible tag locations to two symmetrical points (black and red crosses).

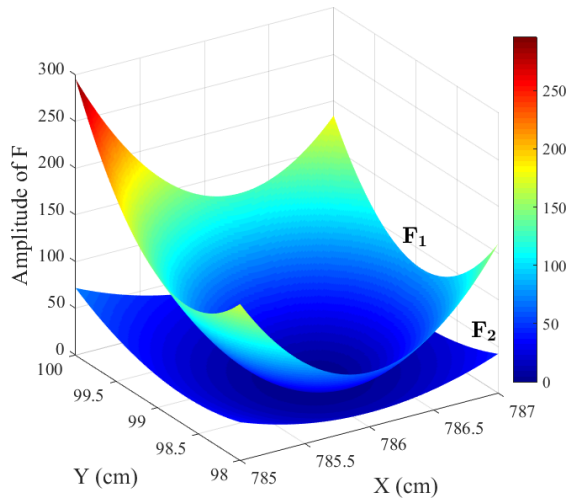


Fig. 5: The curvature of two objective functions, around their global minimum. F_2 is approximately flat in comparison with F_1 , leading to less reliable estimations.

downsampled by a factor of 5. Fig. 5 represents the amplitudes of the two cost functions and compares their curvature around their common solution.

Consider now a displacement from the optimum values, $(x^{opt} + \Delta x, y^{opt} + \Delta y)$. This would increase the amplitude of both cost functions by ΔF_1 and ΔF_2 respectively. Since F_1 is much steeper than F_2 , ΔF_1 would be significantly greater than ΔF_2 . Thus, for the same displacement from the optimum values $\Delta x, \Delta y$, the corresponding fit of F_2 barely changes (i.e. high variance), whilst the fit of F_1 is much worse (i.e. low variance). Notice, that the worse quality of the downsampled set (smaller number of samples) was captured in the curvature of F_2 (nearly flat), leading to higher variance and poor confidence.

The reliability of an estimation strictly depends on the curvature of the objective function; the steeper the curve towards the global minimum, the lower the variance of the solution and thus, the more confident one can be about the estimation. Extending the above observation to the multi-variable function (5), by examining the local curvature with respect to all dimensions, we can evaluate the confidence of each estimated parameter.

The variance of each parameter (x, y, z, c) is given by:

$$\begin{aligned} var_x &= C(1, 1) \\ var_y &= C(2, 2) \\ var_z &= C(3, 3) \\ var_c &= C(4, 4) \end{aligned} \quad (7)$$

where $C(i, i)$ is the i^{th} diagonal element of the covariance matrix C :

$$C = \sigma^2 H^{-1} \quad (8)$$

In (8), σ^2 is the variance of the residuals, defined as the average of the squared differences from the mean and H^{-1} is

the inverse of the 4×4 Hessian matrix of F in (5), computed for the best-fit values $(x^{opt}, y^{opt}, z^{opt}, c^{opt})$:

$$H = \begin{bmatrix} \frac{\partial^2 F}{\partial x^2} & \frac{\partial^2 F}{\partial x \partial y} & \frac{\partial^2 F}{\partial x \partial z} & \frac{\partial^2 F}{\partial x \partial c} \\ \frac{\partial^2 F}{\partial y \partial x} & \frac{\partial^2 F}{\partial y^2} & \frac{\partial^2 F}{\partial y \partial z} & \frac{\partial^2 F}{\partial y \partial c} \\ \frac{\partial^2 F}{\partial z \partial x} & \frac{\partial^2 F}{\partial z \partial y} & \frac{\partial^2 F}{\partial z^2} & \frac{\partial^2 F}{\partial z \partial c} \\ \frac{\partial^2 F}{\partial c \partial x} & \frac{\partial^2 F}{\partial c \partial y} & \frac{\partial^2 F}{\partial c \partial z} & \frac{\partial^2 F}{\partial c^2} \end{bmatrix} \quad (9)$$

The curvature of (5) along each direction is related to its respective second partial derivative. However, the direct computation of all second partial derivatives in (9) can increase the algorithm's complexity and cost. For values near the solution, H can be approximated with

$$H = J^T J \quad (10)$$

where J is the $N \times 4$ Jacobian matrix of phase model (4) and is given by

$$J = \begin{bmatrix} \frac{\partial \phi_1}{\partial x} & \frac{\partial \phi_1}{\partial y} & \frac{\partial \phi_1}{\partial z} & \frac{\partial \phi_1}{\partial c} \\ \frac{\partial \phi_2}{\partial x} & \frac{\partial \phi_2}{\partial y} & \frac{\partial \phi_2}{\partial z} & \frac{\partial \phi_2}{\partial c} \\ \dots & \dots & \dots & \dots \\ \frac{\partial \phi_N}{\partial x} & \frac{\partial \phi_N}{\partial y} & \frac{\partial \phi_N}{\partial z} & \frac{\partial \phi_N}{\partial c} \end{bmatrix} \quad (11)$$

In (11), ϕ_i , $i \in [1, N]$ is the i^{th} sample produced by the theoretical model (4) for the estimated optimum parameters $(x^{opt}, y^{opt}, z^{opt}, c^{opt})$. This is a common approximation used in non linear optimization problems [37], since it provides the possibility to acquire the Hessian matrix only by the computationally inexpensive first partial derivatives. Finally, by exploiting each parameter's variance from (7), we can calculate the confidence interval $CI(\%)$ around each estimated value; typically the 95% confidence interval is used. For example $CI_x(95\%) = 50cm$ means we are 95% confident that the estimated value x^{opt} lies within 50cm from the true one. The broader the length of the confidence interval is, the more certain we can be about the estimation. Hereinafter, $CI(95\%)$ will be referred to as CI .

B. Robot's Trajectory vs. Localization Accuracy

Next, we investigate how the shape of the antenna's trajectory affects the performance of Phase ReLock in 3D localization. More specifically, we wish to correlate the length and curvature of the robot's path with the confidence of the estimations (i.e. the confidence interval of (7)) and consequently with the localization error. We wish to create a realistic simulation model that takes into account inaccuracies, related to the actual data. We consider trajectories with different curvatures along typical indoor geometries. Ideally, for accurate localization,

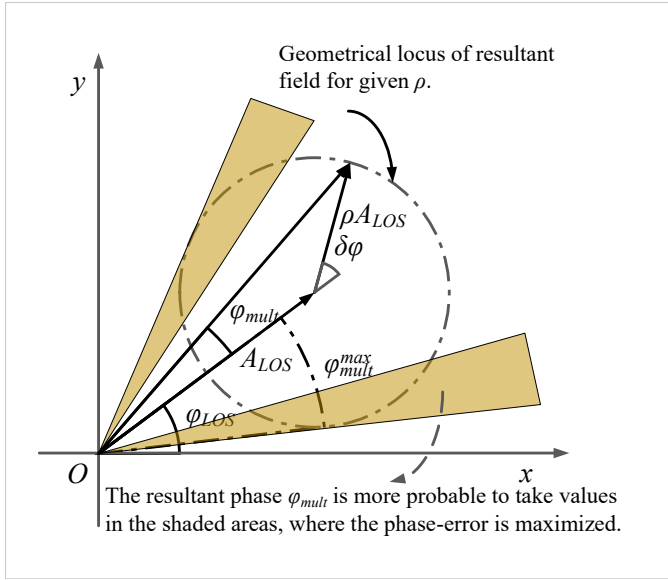


Fig. 6: Representation of the two-ray model, considered in the simulations.

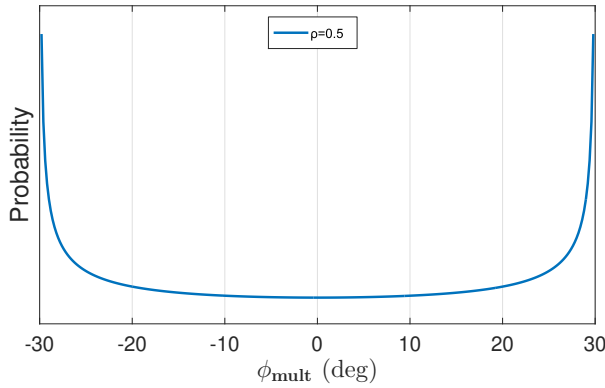


Fig. 7: Probability density function $f_{\phi}(\phi_{mult}|\rho = 0.5)$. The probability increases as the phase takes values near $\phi_{mult}^{max} = \pm 30^{\circ}$.

the reader would measure only the phase of the Line Of Sight contribution. However, the reader actually measures the phase of the resultant vector, produced by the phase-sum of the direct field with all other contributions (multipath). Furthermore, the reader suffers from zero-mean Gaussian Noise.

The unwrapped phase was modeled as

$$\phi = \phi_{LOS} + \phi_{mult} + \phi_{noise} \quad (12)$$

ϕ_{LOS} corresponds to the Line-Of-Sight (LOS) path and is given by (4). ϕ_{noise} represents the noise on measurements and assumed to be of Gaussian nature with a standard deviation of 0.1 rad.

In order to explain the term ϕ_{mult} , which has been introduced to account for multipath, consider the representation shown in Fig. 6. Let $A_{LOS} \cos(\omega t + \phi_{LOS})$ denote the LOS field and $\rho A_{LOS} \cos(\omega t + \phi_{LOS} + \delta\phi)$ the vector sum of all other contributions, referred to as "multipath", where $\rho \leq 1$ (we assume that the direct contribution is stronger than "multipath") and $\delta\phi$ is the phase difference of "multipath"

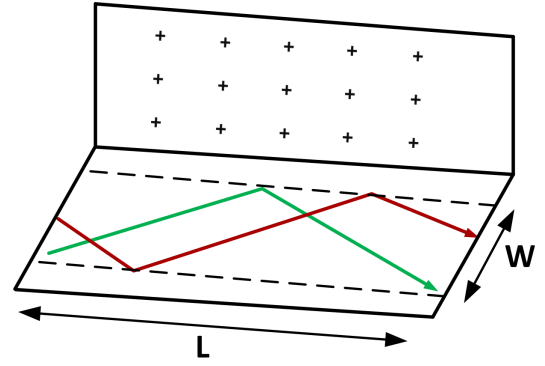


Fig. 8: The types of non straight trajectories that were investigated during the simulations. Single-turned (green) and Double-turned (red). W and L denote the trajectory's lengths along each direction

with respect to the LOS contribution. As represented in Fig. 6, the vector-sum of the LOS plus "multipath" will result in a new vector:

$$A_{LOS} \cos(\omega t + \phi_{LOS}) + \rho A_{LOS} \cos(\omega t + \phi_{LOS} + \delta\phi) \quad (13)$$

with phase:

$$\phi_{LOS} + \phi_{mult}, \text{ where } \phi_{mult} = \tan^{-1} \left(\frac{\rho \sin \delta\phi}{1 + \rho \cos \delta\phi} \right) \quad (14)$$

ϕ_{mult} represents the deviation of the measured phase. Let's consider fixed ratio ρ and $\delta\phi$ a random variable, uniformly distributed in $[0, 2\pi]$; $\rho = 0$ accounts for absence of multipath component, while $\rho = 1$ for equal strength of multipath with LOS. According to this model, the resultant vector, could be anywhere on the circle of Fig. 6 with equal probability. We calculate the probability density function (pdf) of ϕ_{mult} . It can be proven that the corresponding pdf is given by:

$$f_{\phi}(\phi_{mult}|\rho) = \frac{1}{\pi \sqrt{\rho^2 + (\rho^2 - 1) \tan^2 \phi_{mult}}} \quad (15)$$

while the cumulative distribution function is given by:

$$F_{\phi}(\phi_{mult}|\rho) = \frac{2}{\pi} \tan^{-1} \left(\frac{\sqrt{2} \sin \phi_{mult}}{\sqrt{-1 + 2\rho^2 + \cos 2\phi_{mult}}} \right) \quad (16)$$

The maximum phase deviation (from the phase of the LOS component) is (see Fig. 6 for a geometrical explanation):

$$\phi_{mult}^{max} = \pm \tan^{-1} \left(\frac{\rho \sin(\cos^{-1}(-\rho))}{1 - \rho^2} \right) \quad (17)$$

and $\phi_{mult} \in (-\phi_{mult}^{max}, \phi_{mult}^{max})$ in (13). The corresponding plot of the probability density function of ϕ_{mult} for $\rho = 0.5$ is shown in Fig. 7. Notice that the resultant phase is more probable to take values at the regions near $\pm \phi_{mult}^{max}$. The corresponding area is shaded in Fig. 6. A physical interpretation is that those extreme angular regions, include a larger section of the circle, where the resultant field moves with uniform probability. In sharp contrast to the effects of a zero-mean "Gaussian" stochastic error model, which would concentrate the simulated error around the LOS component, the proposed

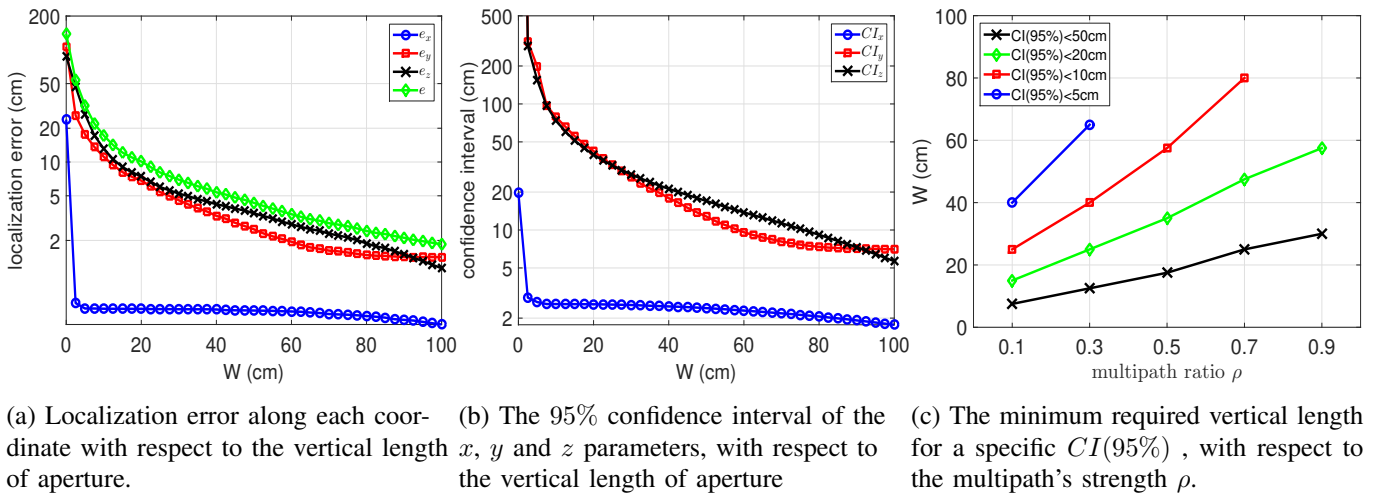


Fig. 9: Simulation results for one turn.

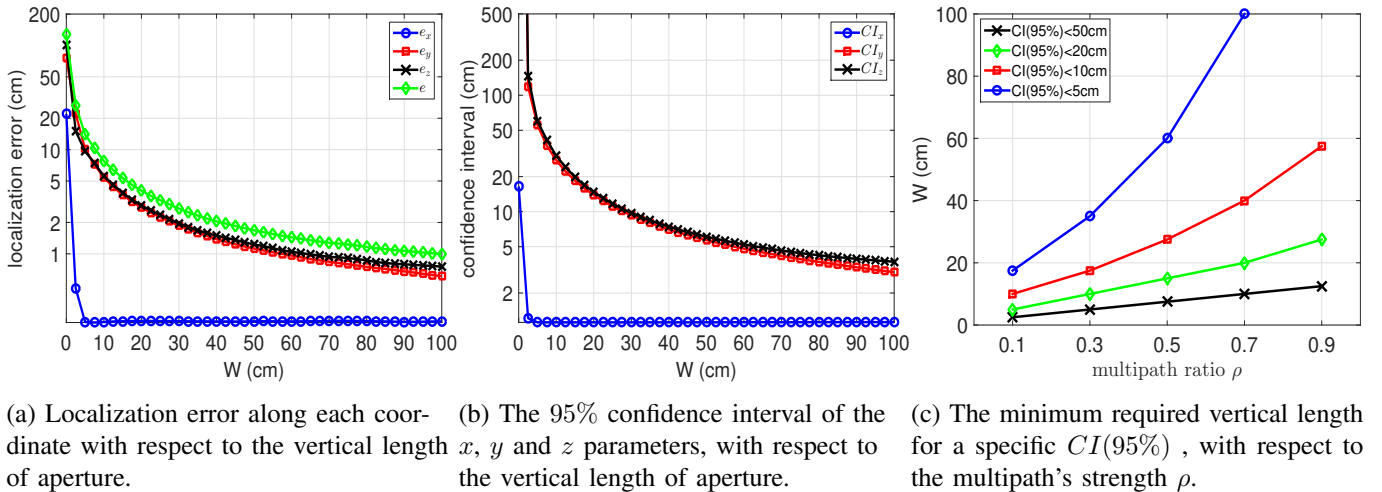


Fig. 10: Simulation results for two turns.

multipath-model is expected to affect significantly the simulated phase values, dragging each sample away from its LOS value.

C. Simulation Results

We simulated a realistic inventorying scenario, according to which, the robot traverses a corridor-type area in two types of trajectories: i) a single-turned, where initially the robot is moving along a straight segment, makes a turn and continues moving to a different direction, and ii) a double-turned trajectory where the robot changes direction twice, by making two turns. Fig. 8 depicts these two shapes, where W denotes for the length of the motion along the y -direction and L along the x . W can quantify the curvature of the examined trajectory, while L remains constant for all simulations. The bigger the value of W is, the more abrupt the occurred turns become (i.e. the relative angle between the corresponding straight sub-paths), leading to a more curved trajectory.

We aim to evaluate and compare the efficiency of the two trajectory-types, under different aperture lengths W and different multipath conditions; ratio ρ in particular. For this

purpose, 15 uniformly distributed tag locations were generated for localization and the results were averaged over 500 iterations. To ensure fairness in the comparison, given that the total length of the trace increases with W , the number of processed measurements for each tag was $N = 200$ in all simulations. The results of Phase ReLock are plotted in Figs. 9 (single rotation) and 10 (two rotations).

Figs. 9 (a) and 10 (a) show the mean estimation error per coordinate-axis and the total 3D error for increasing values of W (up to $1m$) and $\rho = \{0.1, 0.3, 0.5, 0.7, 0.9\}$. Figs. 9 (b) and 10 (b) show the corresponding 95% confidence interval of the estimations, calculated by (7). Notice how well the curve of estimated CI s of Figs (b) match the curve's shape of the calculated mean errors of Figs (a). Since the robot moves along the x axis, the corresponding error is small, even for small values of W . On the contrary, the estimation of y and z coordinate depends on the adequacy of the robot's trajectory; the error and the confidence interval of the estimations decrease as the vertical length of the aperture increases. Hence, the ability of eliminating the rotational symmetry that is formed along the $y - z$ plane (see Fig. 4 (c)) depends on the width

of the trajectory. For a completely straight path, the locus of possible tag locations is a pure circle around the antenna's path. When the shape of the path becomes non straight, the locus is gradually reduced, so does the ambiguity. The more curved the trajectory is (i.e. the bigger it's length), the more confident and proper estimations are made.

In Figs. 9 (c) and 10 (c) we investigate the trajectory's effect on the estimations' confidence for different values of multipath's power. Particularly, we increase the ratio ρ and we seek for the minimum value of length W , for which, a desired level of confidence is achieved. As the strength of the multipath contribution increases, the width of the robot's path should increase in order to achieve a specified reliability. For example, if we request for a confidence interval lower than 20cm (green/diamond marker) for all parameters in an environment with $\rho = 0.9$, the robot's path has to be either a single-turned of length $W = 60cm$ or a double turned of length $W = 30$.

The two-turns trajectory seems to be more efficient when compared against the single-turn. For every value of W , the two-turns path results in better accuracy and confidence. This prevalence is significant especially for small values of W . For instance, when the robot is restricted to move within $W = 10cm$, the estimation's mean error and confidence for a single-turned trajectory is 18cm and 80cm, respectively, whilst the resulted values for the double-turned type are 8cm and 35cm, respectively. This can be critical in cases when the spatial boundaries do not allow for wide robot motions, so equivalently, the robot has to make more turns inside the available space. Furthermore, the double-turned delivers better reliability under the same multipath conditions. In the case of desiring confidence less than 10cm (i.e. $CI(95\%) < 10cm$, red/square marker) for each estimated parameter, the two-turns trajectory with the proper length, can satisfy it for all tested values of ρ , whilst for the one-turn type, $CI < 10cm$ could not be preserved when ρ was higher than 0.7.

IV. EXPERIMENTAL CAMPAIGN

The experiments were conducted inside a lab, in our campus. Our robot, "Frida" (Fig. 1), moved inside the environment, created a 3D map of it, localized itself and then localized all surrounding tags, by applying the proposed method. The successive poses (locations and directions) of the robot, and hence of the antenna's synthetic aperture, were not known, but estimated. This is a **necessary** process, which is expected to increase the localization error, since the error concerning the location of the antenna propagates into the final localization error of the tags.

A. Map Creation and Localization of the Robot's Trajectory

"Frida" is capable of entering any (including unknown) environment, creating a 3D map of it, and localizing itself therein. To accomplish that, measurements from 2D Lidar sensors, 3D Depth Cameras, and odometry sensors are combined and seamlessly fused together by utilizing a Particle Filter [38], a discrete class of Monte Carlo Localisation (MCL) filters [39]. The nature of MCL approaches allows them to

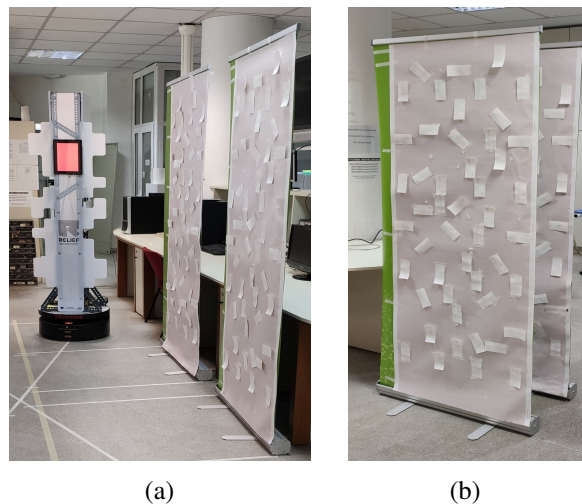


Fig. 11: Photos during the experiments. The banners have been placed (a) side by side and (b) back-to-back

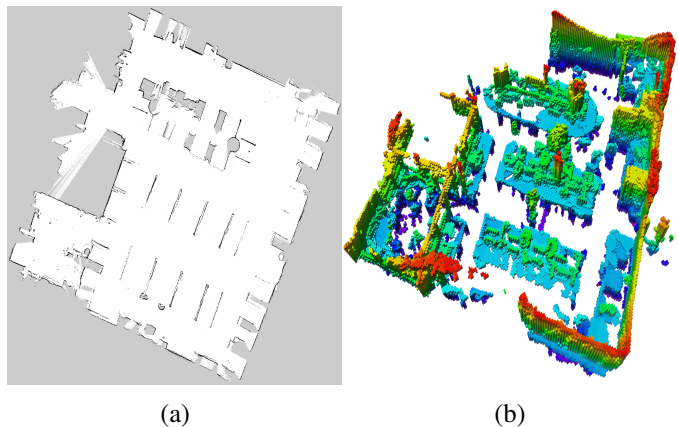


Fig. 12: 2D (a) and 3D (b) map created by "Frida" during an experiment.

represent the uncertainty in the robot's pose by maintaining a set of hypotheses (called particles) not bound to a unimodal probability density function as in Kalman filters [40]. Among others, this representation allows MCL approaches to globally localize a robot within a given map and keep track of pose ambiguities until being able to resolve them by virtue of being able to represent arbitrarily complex probability densities.

In particular, particle filters recursively estimate the posterior of a robot's pose as follows:

$$p(\mathbf{x}_t | \mathbf{z}_{1:t}, \mathbf{u}_{0:t-1}, M) \propto \int_{\mathbf{x}'} p(\mathbf{x}_t | \mathbf{x}', \mathbf{u}_{t-1}) \cdot p(\mathbf{x}' | \mathbf{z}_{1:t-1}, \mathbf{u}_{0:t-2}, M) d\mathbf{x}' \quad (18)$$

Here, the pose of the robot at time t is denoted by \mathbf{x}_t ; $\mathbf{u}_{0:t-1}$ is the sequence of motion commands executed by the robot, and $\mathbf{z}_{0:t}$ is the sequence of observations made by the robot, typically obtained in contemporary robotic practices by 2D range scanners, cameras, sonars or other sensors; M is the map representing the environment in which the robot moves. The motion model $p(\mathbf{x}_t | \mathbf{x}_{t-1}, \mathbf{u}_{t-1})$ denotes the probability

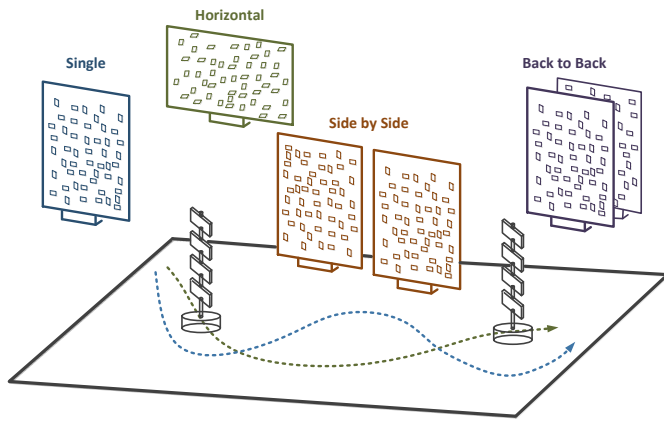


Fig. 13: Representation of the experimental set-up

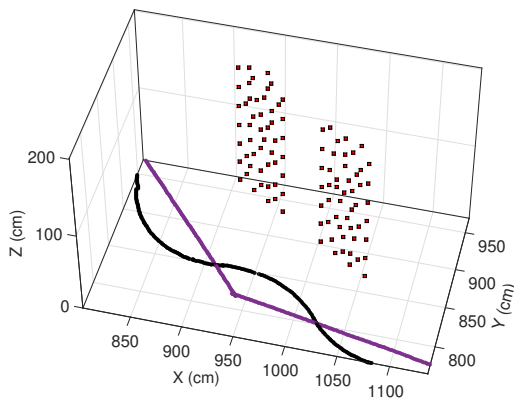


Fig. 14: Robot's trajectories as estimated by the SLAM algorithm, during the "Side by Side" experiment. The slalom-type ("S") is depicted with black color and the single-turned ("V") with purple.

that, at time t , the robot ends up in state \mathbf{x}_t given that it executes the motion command \mathbf{u}_{t-1} while being in state \mathbf{x}_{t-1} at time $t-1$. Typically, in wheeled mobile robots, motion commands are obtained via encoder sensors, and commonly referred to as *odometry*. The observation model $p(z_t | \mathbf{x}_t, M)$ is unique to the operating principle of each sensor and it denotes the likelihood of a given sensor making the observation z_t while the robot is posed at \mathbf{x}_t . Since particle filters maintain a set of different hypotheses as to the state of the robot, each is weighed according to the likelihood that the robot measured z_t under a particle's specific pose hypothesis \mathbf{x}_t^i , where i denotes the index of particle i .

As the robot moved in the area, it constructed an accurate 2D map of the environment, demonstrated in Fig. 12 (a) and a less accurate 3D map, demonstrated in Fig. 12 (b).

B. Measurements

The laboratory environment was full of scatterers such as desks, chairs, racks, lab equipment, etc. 100 passive UHF RFID tags were attached on top of two $2m \times 0.5m$ roll-up banners, as shown in Fig. 11. The tags were placed with random orientations, in order to investigate the effect of different polarizations on the accuracy of the estimations.

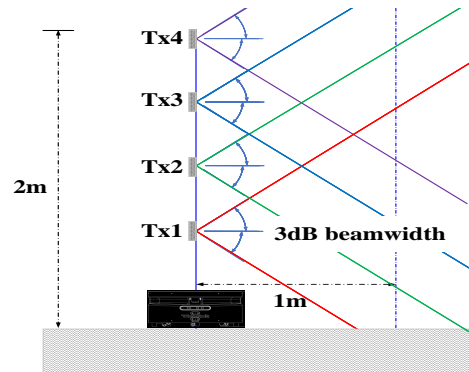


Fig. 15: Each antenna illuminates a different angular region depending on its height and its beamwidth.

Their relative position on each banner was known, since they were attached on millimeter paper, forming an accurate local coordinate systems. The advantage of deploying easy-to-transfer banners is that we were able to move them to different locations and orientations inside the area, in order to investigate the performance of the robot, under different propagation conditions, different tags' densities per m^3 , etc. Measurements were repeated for several configurations: two banners placed side by side, two banners back to back and a single banner placed both vertically and horizontally (see Fig. 13 and Fig. 11). Furthermore, since the designed robot is targeted to navigate inside corridor-type areas (e.g. warehouses, retail stores), we deployed trajectories similar to the ones expected in real applications. Two types of non straight paths were utilized, denoted as "V" and "S", in the following Tables. "V" corresponds to a single turned trajectory (named after its "V" shape), while "S" is a slalom-type trajectory with more direction changes (see Fig. 14). The deployed speed was $2cm/s$. Depending on the geometrical relation between the tag and the antenna, the generated synthetic aperture for each tag, differs in length, number of direction-changes and distance from the banners/tags; the minimum and maximum recorded robot-to-banner distance is $0.5m$ and $1.5m$, respectively.

Moreover, the produced estimations of the tag locations correspond to the map's coordinate system. In order to evaluate the accuracy of any RFID method, both the actual and estimated tag locations have to correspond to the same system. Therefore, we need to pinpoint the locations of the banners inside the 3D map, such that the local coordinate system of the banner's millimeter paper is transformed to the coordinate system of the map. This manual process is not necessary in the actual inventorying application, since the results are directly shown in the map created by the robot, but only for evaluation of the accuracy of the different RFID methods. This procedure is expected to add an error, which will be accumulated to the final localization error.

The robot carries 2 UHF RFID readers and 4 70° half-power beamwidth, circularly polarized UHF RFID antennas per side, thus forming a total of 8 Synthetic Apertures while moving. Depending on the height of each antenna and the robot-to-banner distance, each antenna illuminates a different region

TABLE I: Antenna 1 ($z=0.63\text{m}$)

		Localization Error					
		Initial			for CI<100cm		
experiment	path	mean (cm)	std (cm)	tags	mean (cm)	std (cm)	tags
Back2Back	"V"	$> 10^2$	$> 10^2$	100	39.6	30.8	83
Side2Side	"S"	$> 10^3$	$> 10^4$	100	51.7	56.5	79
Side2Side	"V"	$> 10^3$	$> 10^4$	100	43.3	33	60
Single	"V"	$> 10^4$	$> 10^5$	50	51.5	50.9	43
Horizontal	"S"	44.5	43.5	50	43.5	44.6	46
Horizontal	"V"	52.1	46.2	50	52.1	46.2	50
All experiments					46.5	44.3	361

TABLE II: Antenna 2 ($z=1.07\text{m}$)

		Localization Error					
		Initial			for CI<100cm		
experiment	path	mean (cm)	std (cm)	tags	mean (cm)	std (cm)	tags
Back2Back	"V"	$> 10^2$	$> 10^2$	100	36.3	29.5	94
Side2Side	"S"	$> 10^4$	$> 10^4$	100	37.9	35.2	90
Side2Side	"V"	$> 10^3$	$> 10^4$	100	40.7	52.7	79
Single	"V"	$> 10^2$	$> 10^2$	50	42.2	51.2	49
Horizontal	"S"	66.5	57.3	50	51.6	32.6	42
Horizontal	"V"	76.3	99	50	45	44.9	38
All experiments					40.8	41.1	392

TABLE III: Antenna 3 ($z=1.53\text{m}$)

		Localization Error					
		Initial			for CI<100cm		
experiment	path	mean (cm)	std (cm)	tags	mean (cm)	std (cm)	tags
Back2Back	"V"	$> 10^3$	$> 10^3$	100	55.4	42	91
Side2Side	"S"	$> 10^3$	$> 10^4$	100	46.5	35.8	82
Side2Side	"V"	$> 10^2$	$> 10^3$	100	42	41.5	71
Single	"V"	$> 10^4$	$> 10^4$	50	37.2	37	45
All experiments					48.8	39.8	289

TABLE IV: Antenna 4 ($z=1.93\text{m}$)

		Localization Error					
		Initial			for CI<100cm		
experiment	path	mean (cm)	std (cm)	tags	mean (cm)	std (cm)	tags
Back2Back	"V"	$> 10^3$	$> 10^4$	100	63.4	54	73
Side2Side	"S"	$> 10^4$	$> 10^5$	100	65.6	64.7	61
Side2Side	"V"	$> 10^3$	$> 10^4$	100	43	37	53
Single	"V"	$> 10^4$	$> 10^4$	50	39.7	26.7	34
All experiments					55.6	51.7	221

of the banner, collecting more measurements from tags placed in the corresponding region and less from others. This effect is shown in Fig. 15. Tags placed at the very bottom (/top) of the banner will not be well identified by the upper (/lower) antennas. Similarly, tags placed at the central area allow for a sufficient set of measurements from all tags. In any case, the localization problem was solved for all tags no matter what the number of obtained measurements was.

C. Experimental Results

We deployed Phase ReLock for each antenna **independently**, as described in Section II. Tables I-IV summarize the

localization results, for each experiment and each antenna. The column corresponding to the initial localization error indicates a huge mean error and standard deviation. Measurements of tags that are placed much higher or lower than the antenna's height are expected to be inadequate for decent localization. Furthermore, although the robot was forced to move in non straight trajectories, it is more than possible for a tag to be in the reading-range of the antenna only during a specific part of its path, which either is straight or not "wide enough" (refer to Section III). Consequently, the estimations based on such problematic data will lead to a huge increase of the localization error.

As for the horizontally arranged banner, the maximum height of any tag was only 0.5m; i.e. quite lower than the two upper antennas of the robot. Therefore, the experiment was repeated only for Antenna 1 and 2, since Antenna 3 and 4 would not have collected a sufficient number of measurements from any of the tags (see Fig. 15). The fact that the space of interest was not spread in height, in combination with the lower tag-density of the setup (half of the tags' population, while those tags are spread along the direction of motion), led to an adequate collection of measurements from both antennas. Hence, the initial performance in this experiment is good and the localization metrics are not disturbed by "error-outliers" as in other experiments.

D. Characterization of the method

Fig. 16 compares two tag estimations. It represents the objective function (5) for two tags, that have been detected by Antenna 1, during different parts (green) of the robot's whole trajectory (black). The amplitudes of (5) have been normalized with respect to the maximum recorded value. The 2D slices are through the estimated tag's location and extend to an area of $\pm 50\text{cm}$ around the estimated solution. The synthetic aperture for tag A has sufficient length for both x and y direction, allowing for an accurate localization. On the contrary, measurements of tag B were collected only by a short part of the robot's path. As a result, the estimation of tag B is worse, in terms of both accuracy and confidence. The presence of hotter colors in (a) indicates that (5) increases more abruptly than in (b), for values of X, Y, Z around the solution. Notice also that the calculated confidence intervals of the variance (7) for each parameter are much narrower for Tag A, implying better reliability.

Fig. 17 addresses this issue, as well. It depicts the increase of the cost function F , as the parameter values (x, y, z) change away from the optimum ones, along each axis-direction; the amplitudes have been again normalized. In all cases, the shapes corresponding to tag A are much steeper in comparison with the respective shapes of Tag B. This indicates smaller variance for every estimated parameter and hence, greater confidence for Tag A. It is worth noting that the curve of Fig. 17 (c) of Tag A is not convex, but features two local minima. This effect is expected, due to the symmetry with respect to the antenna's height, as discussed earlier. The vertical dashed line represents the relative height of the antenna with respect to the estimated z^{opt} of Tag A.

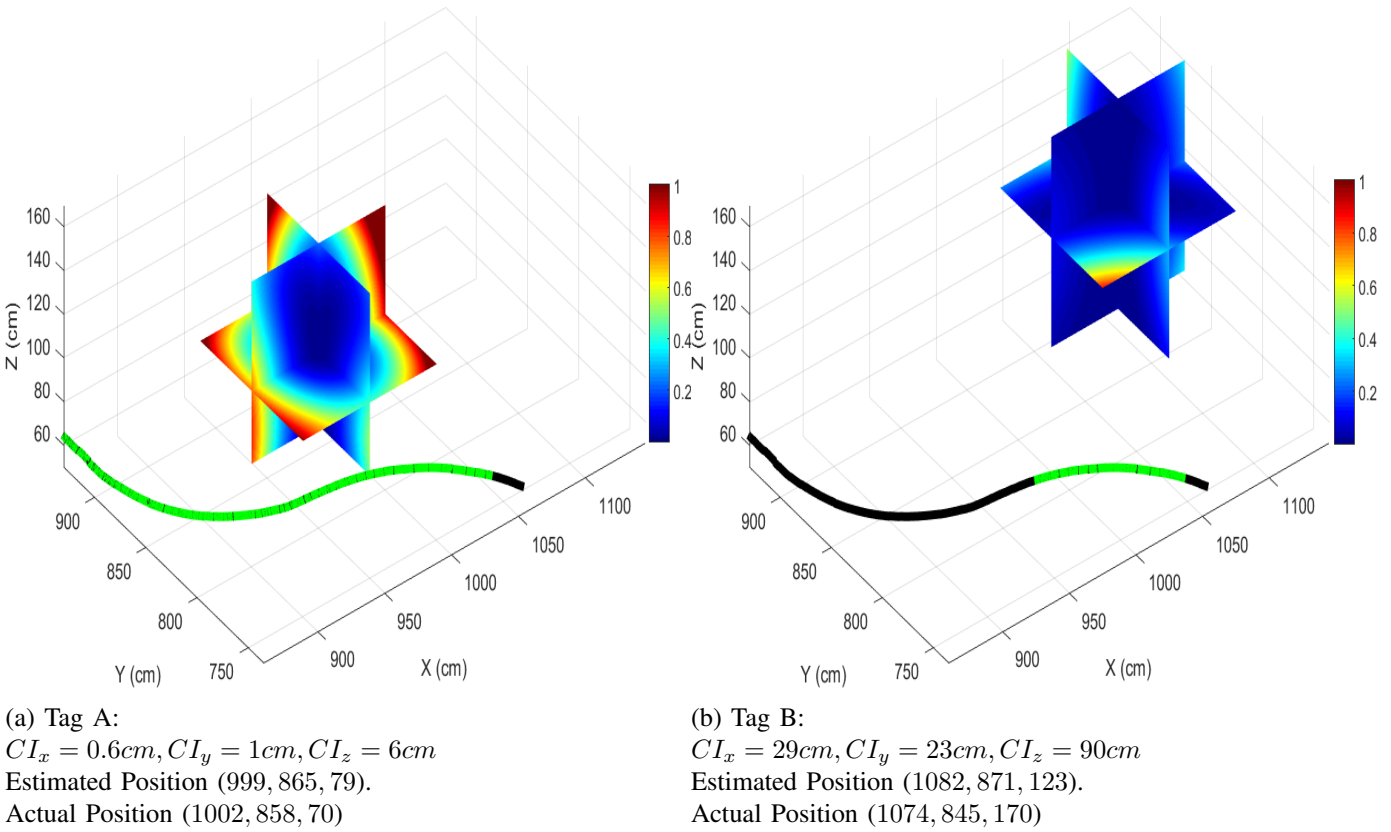


Fig. 16: 3D representation of (5) for two different tags. The robot’s trajectory is depicted with black colour, while the measurements processed (synthetic aperture) with green.

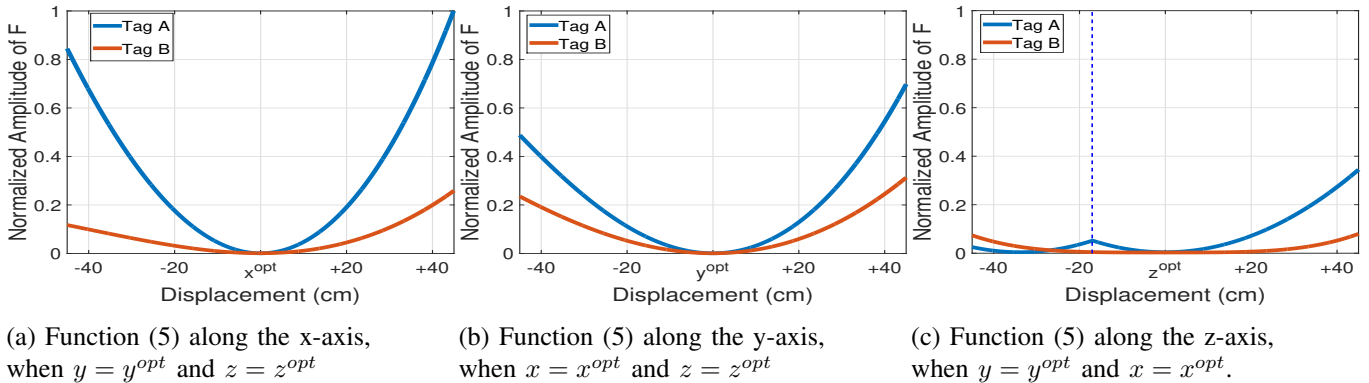


Fig. 17: Curvature of function (5), along x,y and z parameter direction, for the tags of Fig. 16.

So when the robot’s trajectory is unsuitable, or only few data are available, the ambiguity of the estimated solution would be highly increase. This property will be mapped in the curvature of (5) and consequently in the parameter’s variance calculated by (7). Therefore, we exploit the confidence interval ($CI(95\%)$) of the variance to reject such poor estimations. More specifically, by demanding this proposed metric to be lower than a desired threshold, we account only for estimations that are considered reliable enough. Equivalently, an estimation is considered unreliable/poor when at least one of its parameter has confidence interval greater than the defined threshold. The last column of Tables I-IV, indicates the dramatic improvement of the method’s accuracy, when

uncertain estimations with $CI > 100cm$, are rejected.

The mean error from all experiments and antennas was in the order of 50cm. This value is quite small compared to the actual search volume; due to the length of the robot’s motion in each experiment (i.e. around 3m), the reading-range of the reader (i.e. around 7m) and the height of the banner (i.e. 2m), the size of the total search volume is around $42m^3$. The final achieved accuracy is quite satisfactory, also considering that the 3D problem was solved by a single antenna, the robot’s trace was not known (but estimated), the considered actual locations of the tags (ground truth) suffer from errors in the order of cm , the environment is full of scatterers (multipath-rich) and the solution was sought in 3D space and not along

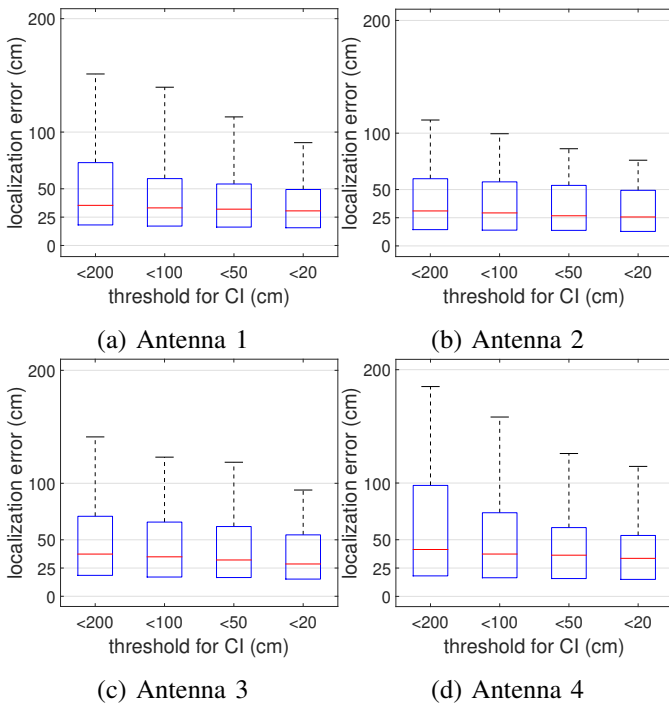


Fig. 18: Localization error for all experiments, when different thresholds are used to reject unconfident estimation. The 25th, 50th, 75th and 99th percentiles of the error are presented.

TABLE V: Estimation-Time

			Antenna			
			1	2	3	4
experiment	path	tags	execution time (sec)			
Back2Back	"V"	100	8.7	9	7.8	11
Side2Side	"S"	100	9.	9.2	10.2	10.1
Side2Side	"V"	100	11.3	10.3	11.2	11.3
Single	"V"	50	5.1	4.8	5.2	6.3
Horizontal	"S"	50	5	4.8		
Horizontal	"V"	50	4.9	4.8		
All Experiments			44	42.9	34.4	38.7

a given horizontal cut.

1) *Applying different confidence thresholds*: Fig. 18 examines the deployment of different values for the desired confidence interval CI; each plot corresponds to each antenna and the results are averaged over the total of experiments. In particular, it presents the 25th, 50th, 75th and 99th percentile of the localization error, when estimations, whose confidence interval is wider than 200cm, 100cm, 50cm and 20cm, are dismissed. As we set stricter constraints with respect to the achieved confidence (i.e. as the threshold of CI decreases), extreme values of error are removed, leading to a decrease of the reported localization error, at the cost of course of reduced number of localized tags.

E. Algorithm's Execution Time

It's worth noting that estimations per experiment were drawn in a few seconds, processing approximately 20000 measured samples collected during 3 minutes of robot's motion; the estimation-time is much smaller than the collection-time.

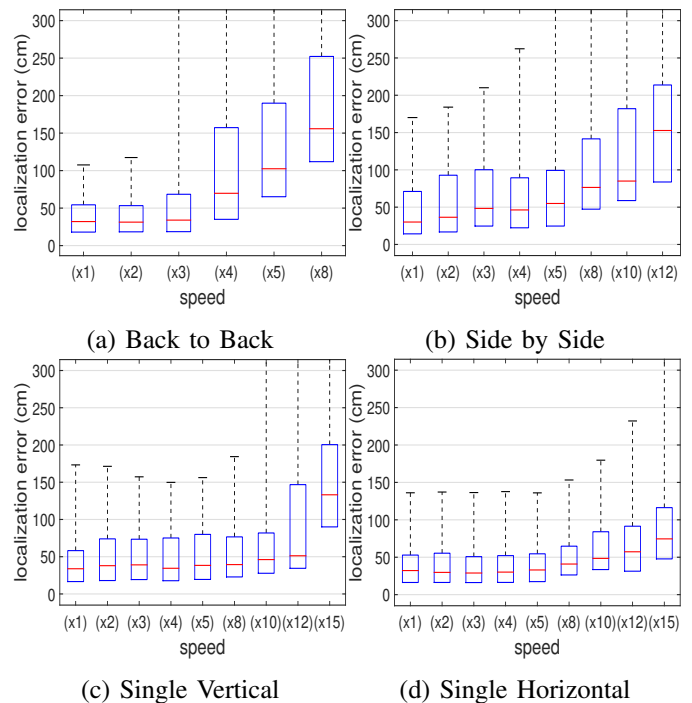


Fig. 19: Localization error of Antenna 1, for multiples of the original robot speed, for each experiment. The 25th, 50th, 75th and 99th percentiles of the error are presented.

Table V presents the estimation times for each antenna and experiment. For example, by exploiting data from Antenna 1, Phase ReLock accomplished to localize 450 tags in less than 45 seconds, dedicating about 100ms to each tag. The execution-time is quite impressive, especially when compared to the speed of state-of-the-art grid-based methods. Analytical comparisons can be found in [28] and [29] for the two and three dimensional problem, respectively. In [29] particularly, where the core algorithm of the proposed method is same as herein, the grid-based methods and Phase ReLock delivered equivalent accuracy, however the latter performed 360 times faster.

F. Performance vs Robot's Speed

Next we investigate the influence of the robot's speed over the localization ability of Phase ReLock. The sampling rate of the antenna and the density of the collected measurements depend on the speed of the robot and the tag population within range. Due to the random-medium-access nature of the slotted Aloha protocol, the collision probability increases as the number of the competing tags increases. Hence, the tag density of the set-up is expected to play an important role for the performance of the method, as the speed increases.

As described in Section IV-B, the easy-to-transfer banners allow for testing multiple spatial configurations. Each set up corresponds to a different tag density per space unit. As a result the robot's speed is expected to affect the performance at each experiment differently. By downsampling the available collected data, we can consider higher speeds; e.g. by taking

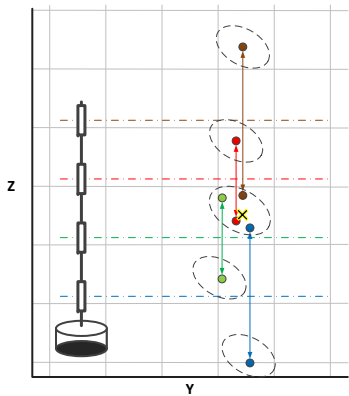


Fig. 20: The possible tag locations (colored circles) by exploiting all four antennas and the created clusters (circled dashed lines). The tag (cross) is expected to be in the most populated cluster.

1 of every 2 measured samples, an equivalent speed, twice as high as the original one, can be assumed.

Fig. 19 validates the performance of Antenna 1 for increasing speed values. We tested values that are multiples (double, triple and so on) of the one experimentally deployed, i.e. 2cm/s . So in Fig. 19, ($\times 2$) corresponds to a speed of 4cm/s , ($\times 3$) to a speed of 6cm/s and so on. In general, the performance deteriorates as the speed increases but in different rate for each experiment. The worst case scenario is the one with two banners placed back to back (Fig. (a)), where the maximum tag density is obtained. The accuracy is comparable for the two lower speed multiples (i.e. ($\times 2$) and ($\times 3$)), but then the error rapidly increases until there are no adequate data left for the method to process. Therefore, the maximum speed the robot for this setup, would be 16cm/s . On the contrary, when only one banner is placed either vertically (Fig. (c)) or horizontally (Fig. (d)), the tag-density is much smaller. Speed multiples that are lower than ($\times 8$), hardly affect the method's performance, while the available data are enough for Phase ReLock to be successfully executed, for speeds up to ($\times 15$) the original one; a potential maximum speed for these experiments would be 30cm/s . Of course, in case of such higher speeds, other issues will emerge, regarding the robot's stabilization, safe-navigation, etc.

V. EXTENSION TO MULTI-ANTENNA ROBOTS

We extend the proposed solution, assuming measurements from additional synthetic apertures; i.e. the robot is equipped with multiple antennas at different heights. Initially, each antenna and its measurements are treated independently. Assuming non-straight trajectories and no prior knowledge of tag's height, "Phase ReLock" estimates a pair of possible coordinates per antenna. These are symmetrical with respect to the antenna's height, as shown in Fig. 20 for a total of 4 antennas. Ideally, one point of each pair would coincide with the actual tag's location. However, since the locations have been estimated with error, one can only expect that the points that lay on the correct half-planes will be close to the real

TABLE VI: Multi-Antenna Combination

experiment	path	cost (s)	mean (cm)	std (cm)
Back2Back	"V"	12.3	34.2	25.1
Side2Side	"S"	12.5	31	37
Side2Side	"V"	10.4	31.3	30.6
Single	"V"	7	34.1	30
Horizontal	"S"	4	45.2	27.7
Horizontal	"V"	4.2	50	31
All experiments			34.8	28.2

location, whilst the ones belonging to the wrong half-planes will lay far away from it.

One can deploy any clustering approach, or ideally, calculate all combinations of solutions from the different antennas and select the one that minimizes the sum of the inter-points distances. We deploy the **k-means algorithm** to classify each candidate point to a cluster. The points that are close to the true tag's location will also be close to each other and hence, they will be grouped together. On the contrary, the ones that lay at significant distance from the rest points will be grouped alone, forming clusters of one point. The tag's location is then estimated as the center of the most populated cluster.

Applying the above to the example of Fig. 20, the generated clusters are marked as dashed circles. The actual tag's location is expected in the central cluster of the figure, where 4 solutions from the 4 different antennas are in close vicinity.

We have applied k-means in the experimental results, whenever estimations by at least two antennas were available, after discarding bad estimations with wide confidence interval, $CI > 100\text{cm}$. As a consequence, there are not always four available antenna-solutions for every tag, and k-means is deployed only for the remaining, yet reliable ones. Table VI recaps the final localization results per experiment. As expected, by exploiting more than one antennas, the performance is improved in the order of tens of cm , compared to the respective results of Tables I-IV. The proposed method accomplished localization with a mean 3D accuracy of 35cm . As for the speed of the proposed solution, the computational cost (in secs) introduced by the clustering algorithm, is not important. The estimation-time remained significantly smaller than the measurements' time.

Finally, Fig. 21 distinguishes the estimations according to the number of available antenna-solutions and compares the performance when 2, 3 and 4 antennas were available. The accuracy of the clustering algorithm increases proportionally to the number of antennas exploited. For instance, when all four antennas were available, a median error of about 20cm is achieved, whilst when only two out of four antennas were involved, the median error is double.

VI. CONCLUSION

In this paper, we have shown that by adjusting the motion strategy of the robot, we can accomplish 3D localization of RFID tags even by a single antenna. We have introduced a metric for real-time assessment of the 3D localization-error, based on calculating the Hessian matrix at the minimum of

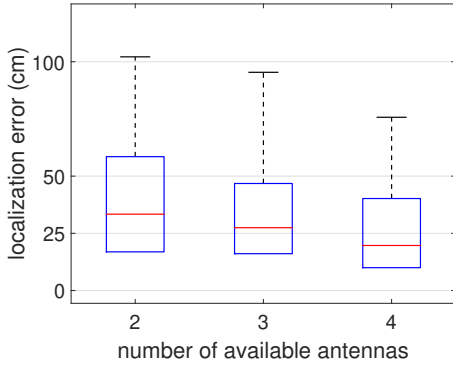


Fig. 21: Performance of clustering algorithm in relation to the number of available single-antenna-based solutions. The 25th, 50th, 75th and 99th percentiles of the error are presented.

the cost function. We have used the prototype metric in the experiments to discard estimations with low expected accuracy and successfully improved the overall localization accuracy.

Furthermore, it was shown that the 3D localization accuracy by a single antenna can be significantly improved by increasing the width and number of turns of the trajectory of the robot. We have introduced a realistic phase model under multipath conditions and derived the closed form probability and cumulative density function of the resultant phase, treating the ratio of the magnitude of multipath contributions to the magnitude of the direct ray as an input variable to the model.

The proposed method has been extended to multiple-antenna configurations; i.e. when measurements from more than one antenna are available. Extensive measurements in an indoor environment involving 6 setups and 450 tags demonstrated a mean estimation error of 35cm, including errors originating from the SLAM process of the robot as well as the uncertainty of the actual locations of the tags in the environment. The estimation-time of the method is orders of magnitude faster than the measurements' time.

The achieved 3D accuracy is adequate for most inventorying applications in large warehouses or retail stores; except perhaps for pick-and-place robots, where mm accuracy is desired. However, further improvement of Phase ReLock is expected, by jointly exploiting measurements from multiple antennas, whenever available, and not independently as deployed herein.

APPENDIX

The following analysis proves theoretically that when two non parallel straight paths are merged, the solution of the 3D localization problem is reduced to two symmetrical points.

Let a tag placed at the unknown point $K(x_k, y_k, z_k)$ and an antenna moving along a known line l_1 , as shown in Fig. 22 (a). The perpendicular straight-segment l_3 that joins K and l_1 is unique and crosses l_1 at the unique point A . Let R_1 be the distance between K and A . R_1 is considered known; already estimated without source of error. For simplicity, x-axis is defined to coincide with line l_1 . Consider the vectors \vec{v}_1 and \vec{v}_3 that are collinear to l_1 and l_3 respectively. Then:

- $\vec{v}_1 = (\Delta x_1, 0, 0)$, $\Delta x_1 = x_{1,0} - x_1 \neq 0$

- $\vec{v}_3 = (x_k - x_1, y_k, z_k)$

We have:

$$\vec{v}_1 \perp \vec{v}_3 \Rightarrow \vec{v}_1 \cdot \vec{v}_3 = 0$$

$$\Rightarrow \Delta x_1(x_k - x_1) = 0 \Rightarrow x_k = x_1 \quad (a)$$

$$|\vec{v}_3| = R_1 \Rightarrow \sqrt{(x_k - x_1)^2 + y_k^2 + z_k^2} = R_1 \Rightarrow$$

$$\sqrt{y_k^2 + z_k^2} = R_1 \quad (b)$$

Notice that (b) corresponds to a circle C_1 around l_1 , with center A and radius R_1 , as shown in Fig. 22 (b). This circle is actually the locus of possible tag locations.

Let now a second antenna array along the known line l_2 , which also lays on plane $z = 0$ (Fig. 22 (a)). Similarly, there is a unique straight-segment, denoted as l_4 , that joins K and l_2 and is perpendicular to l_2 . Let B the unique point of intersection and R_2 the known distance between K and B . Lines l_2 and l_4 are represented by the collinear to them vectors, denoted as \vec{v}_2 and \vec{v}_4 respectively:

- $\vec{v}_2 = (\Delta x_2, \Delta y_2, 0)$, $\Delta x_2 = x_{2,0} - x_2$, $\Delta y_2 = y_{2,0} - y_2$

- $\vec{v}_4 = (x_k - x_2, y_k - y_2, z_k)$

We have:

$$\vec{v}_2 \perp \vec{v}_4 \Rightarrow \vec{v}_2 \cdot \vec{v}_4 = 0 \Rightarrow$$

$$\Delta x_2(x_k - x_2) + \Delta y_2(y_k - y_2) = 0 \Rightarrow$$

$$y_k = C, \quad \text{where} \quad C = \frac{\Delta y_2 y_2 - \Delta x_2(x_1 - x_2)}{\Delta y_2} \quad (c)$$

$$|\vec{v}_4| = R_2 \Rightarrow \sqrt{(x_k - x_2)^2 + (y_k - y_2)^2 + z_k^2} = R_2 \quad (d)$$

Eq. (d) represents a second circle C_2 , with radius R_2 and center B . By substituting (a) and (c) in (d):

$$\sqrt{(x_1 - x_2)^2 + (C - y_2)^2 + z_k^2} = R_2 \Rightarrow$$

$$z_k = \pm D, \quad \text{where} \quad D = (R_2^2 - (C - y_2)^2 - (x_1 - x_2)^2)$$

Notice that x_k and y_k are unique, whilst z_k can take two values, which correspond to two symmetrical solutions, K_1 or K_2 . K_1 and K_2 are symmetrical in relation to $z = 0$ plane; in general they are symmetrical to the $z = z_i$ plane, where z_i denotes for the antenna's height. Fig. 22 (b) represents points K_1 and K_2 as the intersection of circles C_1 and C_2 .

REFERENCES

- [1] RELIEF project, "http://relief.web.auth.gr/", last accessed on January 30 2020
- [2] P. V. Nikitin, R. Martinez, S. Ramamurthy, H. Leland, G. Spiess, and K. V. S. Rao, "Phase Based Spatial Identification of UHF RFID Tags," *2010 IEEE International Conference on RFID*, Orlando, Florida, 2010.
- [3] J. Zhou, H. Zhang, and L. Mo, "Two-dimension Localization of Passive RFID Tags Using AOA Estimation," *2011 IEEE Instrumentation and Measurement Technology Conference (I2MTC)*, Binjiang, China, 2011.
- [4] S. Azzouzi, M. Cremer, U. Dettmar, R. Kronberger, and T. Knie, "New Measurement Results for the Localization of UHF RFID Transponders Using an Angle of Arrival (AoA) Approach," *2011 IEEE International Conference on RFID*, Orlando (FL), 2011.
- [5] S. Subedi, E. Pauls, and Y. D. Zhang, "Accurate Localization and Tracking of a Passive RFID Reader based on RSSI Measurements," *IEEE Journal of Radio Frequency Identification*, vol. 1, no. 2, pp. 144-54, 2017.

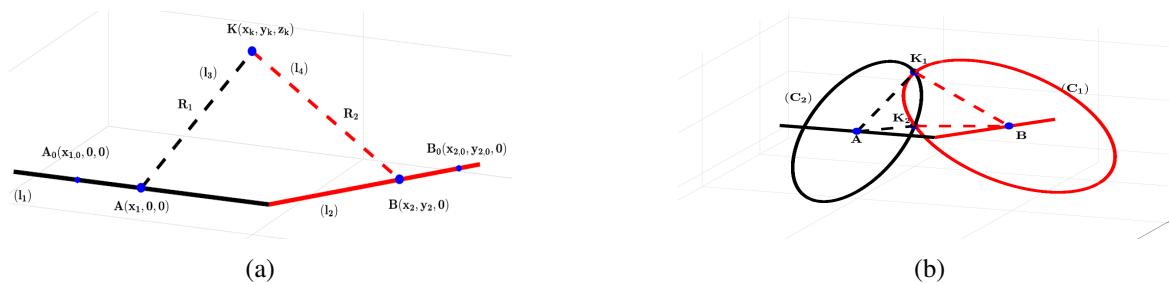


Fig. 22: (a) Geometry of the virtual antenna arrays. (b) Tag's location as intersection of the two circular loci.

- [6] J. Zhang, Y. Lyu, J. Patton, S.C. G. Periaswamy, and T. Roppel, "BFVP: A Probabilistic UHF RFID Tag Localization Algorithm Using Bayesian Filter and a Variable Power RFID Model," *IEEE Transactions on Industrial Electronics*, vol. 65, no. 10, pp. 8250-8259, 2018.
- [7] P. Yang, and W. Wu, "Efficient Particle Filter Localization Algorithm in Dense Passive RFID Tag Environment," *IEEE Transactions on Industrial Electronics*, vol. 61, no. 10, pp. 5641-5651, 2014.
- [8] J. Wang, and D. Katabi, "Dude, Where's my Card?: RFID Positioning that Works with Multipath and Non-line of Sight," *Proceedings of the ACM SIGCOMM 2013 conference on SIGCOMM*, pp. 51-62, Hong kong, China, 2013.
- [9] A. Almaaitah, K. Ali, H. S. Hassanein, and M. Ibnkahla, "3D passive tag localization schemes for indoor RFID applications," 2010 IEEE International Conference on Communications, pp. 1-5, 2010.
- [10] F. Tlili, N. Hamdi, and A. Belghith, "Accurate 3D localization scheme based on active RFID tags for indoor environment," *IEEE RFID-TA*, 2012, pp. 378-382.
- [11] T. Liu, L. Yang, Q. Lin, Y. Guo, and Y. Liu, "Anchor-free backscatter positioning for RFID tags with high accuracy," *IEEE INFOCOM*, 2014, pp. 379-387.
- [12] O. Frey, C. Magnard, M. Ruegg, and E. Meier, "Focusing of airborne synthetic aperture radar data from highly nonlinear flight tracks," *IEEE Trans. Geosci. Remote Sens.*, vol. 47, no. 6, pp. 1844-1858, Jun. 2009.
- [13] Y. Zhang, L. Xie, Y. Bu, Y. Wang, J. Wu, and S. Lu, "3-Dimensional Localization via RFID Tag Array," 2017 IEEE 14th International Conference on Mobile Ad Hoc and Sensor Systems, 2017.
- [14] L. Qiu, Z. Huang, N. Wirstrom, and T. Voigt, "3DinSAR: Object 3D Localization for Indoor RFID Applications," *IEEE International Conference on RFID (RFID)*, 2016.
- [15] R. Miesen, F. Kirsch, and M. Vossiek, "UHF RFID localization based on synthetic apertures," *IEEE Transactions on Automation Science and Engineering*, vol. 10, no. 3, pp. 807-815, 2013.
- [16] L. Yang, Y. Chen, X.-Y. Li, C. Xiao, M. Li, and Y. Liu, "Tagoram: real-time tracking of mobile rfid tags to high precision using cots devices," In *Proceedings of the 20th annual international conference on Mobile computing and networking*, pp. 237-248, 2014.
- [17] L. Shanguan and K. Jamieson, "The design and implementation of a mobile rfid tag sorting robot," In *Proceedings of the 14th Annual International Conference on Mobile Systems, Applications, and Services*, pp. 31-42, 2016.
- [18] A. Buffi, A. Motroni, P. Nepa, B. Tellini, and R. Cioni, "A SAR-based measurement method for passive-tag positioning with a flying UHF-RFID Reader," *IEEE Transactions on Instrumentation and Measurement*, vol. 68, no. 3, MARCH 2019.
- [19] A. Tzitzis, S. Megalou, S. Siachalou, T. Yioultsis, A. Kehagias, E. Tsardoulas, A. Filotheou, A. Symeonidis, L. Petrou and A. G. Dimitriou, "Phase ReLock - Localization of RFID Tags by a Moving Robot," 13th European conference on Antennas and Propagation, Krakow, Poland, 2019.
- [20] A. Motroni, P. Nepa, P. Tripicchio, M. Unetti, "A Multi-Antenna SAR-based method for UHF RFID Tag Localization via UGV", 2018 IEEE International Conference on RFID Technology & Application (RFID-TA), Macau, China, 2018.
- [21] F. Martinelli, "A Robot Localization System Combining RSSI and Phase Shift in UHF-RFID Signals," *IEEE Transactions on Control Systems Technology*, vol. 23, no. 5, pp. 1782-1796, 2015.
- [22] E. DiGiampaolo, F. Martinelli, "A Robotic System for Localization of Passive UHF-RFID Tagged Objects on Shelves," *IEEE Sensors Journal*, vol. 18, no. 20, pp. 8558-8568, 2018.
- [23] L. M. Ni and Y. Liu, "LANDMARC: indoor location sensing using active RFID," *Wireless Networks*, 10(6), pp. 701-10, 2004.
- [24] S. Megalou, A. Tzitzis, S. Siachalou, T. Yioultsis, J. Sahalos, E. Tsardoulas, A. Filotheou, A. Symeonidis, L. Petrou, A. Bletsas, A. G. Dimitriou, "Fingerprinting Localization of RFID tags with Real-Time Performance-Assessment, using a Moving Robot," 13th European Conference on Antennas and Propagation, Krakow, Poland, March 2019.
- [25] S. Siachalou, S. Megalou, A. Tzitzis, E. Tsardoulas, A. Bletsas, J. Sahalos, T. Yioultsis, A. G. Dimitriou, "Robotic Inventorying and Localization of RFID Tags, Exploiting Phase-Fingerprinting," 2019 IEEE International Conference on RFID-Technology and Applications, RFID-TA 2019, Pisa, Italy, September 2019.
- [26] J. Wang and D. Katabi, "Dude, where's my card?: RFID positioning that works with multipath and non-line of sight," *Proceedings of the ACM SIGCOMM 2013 conference on SIGCOMM*, Hong kong, China, pp. 51-62, 2013.
- [27] Y. Ma, N. Selby, F. Adib, "Minding the billions: ultra-wideband localization for deployed RFID tags," *MobiCom 2017, 23rd Annual Conference on Mobile Computing and Networking*, Utah, USA, 2017.
- [28] A. Tzitzis, S. Megalou, S. Siachalou, E. Tsardoulas, A. Kehagias, T. Yioultsis, A. G. Dimitriou, "Localization of RFID Tags by a Moving Robot, via Phase Unwrapping and Non-Linear Optimization," *IEEE Journal of Radio Frequency Identification*, vol 3, no. 4, pp. 216-226, Dec. 2019.
- [29] A. Tzitzis, S. Megalou, S. Siachalou, E. Tsardoulas, T. Yioultsis, A. G. Dimitriou, "3D Localization of RFID Tags with a Single Antenna by a Moving Robot and Phase ReLock," 2019 IEEE International Conference on RFID-Technology and Applications, RFID-TA 2019, Pisa, Italy, September 2019.
- [30] Binmore, Ken; Davies, Joan (2007). "Calculus Concepts and Methods", Cambridge University Press. p. 190. ISBN 978-0-521-77541-0. OCLC 717598615, 2007.
- [31] D.R. Cox, D.V. Hinkley, "Theoretical Statistics", Chapman & Hall, p49, p209, 1974.
- [32] M. A. Branch, T. F. Coleman, and Y. Li, "A Subspace, Interior, and Conjugate Gradient Method for Large-Scale Bound-Constrained Minimization Problems," *SIAM Journal on Scientific Computing*, vol. 21, no. 1, pp. 1-23, 1999.
- [33] R. H. Byrd, R. B. Schnabel, and G. A. Shultz, "Approximate Solution of the Trust Region Problem by Minimization over Two-Dimensional Subspaces," *Mathematical Programming*, vol. 40, pp. 247-263, 1988.
- [34] J. J. More and D. C. Sorensen, "Computing a Trust Region Step," *SIAM Journal on Scientific and Statistical Computing*, vol. 3, pp. 553-572, 1983.
- [35] D. Marquardt, "An Algorithm for Least-Squares Estimation of Nonlinear Parameters," *SIAM J. Appl. Math.*, vol. 11, pp. 431-441, 1963.
- [36] K. Levenberg, "A Method for the Solution of Certain Problems in Least Squares," *Quart. Appl. Math.*, vol. 2, pp. 164-168, 1944.
- [37] V. Buljak, "Optimization Algorithms" in *Inverse Analyses with Model Reduction*, 1st Ed., 2012.
- [38] Sebastian Thrun, Wolfram Burgard, and Dieter Fox, "Probabilistic Robotics" (Intelligent Robotics and Autonomous Agents), The MIT Press, 2005.
- [39] F. Dellaert, D. Fox, W. Burgard and S. Thrun, "Monte Carlo localization for mobile robots," *Proceedings 1999 IEEE International Conference on Robotics and Automation (Cat. No.99CH36288C)*, Detroit, MI, USA, 1999, pp. 1322-1328 Volume 2, doi: 10.1109/ROBOT.1999.772544.
- [40] P. Maybeck, "Stochastic Models, Estimation and Control", Volume 1, Academic Press, New York, 1979.